A MAP-Based Approach for Hyperspectral Imagery Super-Resolution

Hasan Irmak, Gozde Bozdagi Akar, *Senior Member, IEEE*, and Seniha Esen Yuksel, *Member, IEEE*

***Abstract*— In this paper, we propose a novel single image Bayesian super-resolution (SR) algorithm where the hyperspectral image (HSI) is the only source of information. The main contribution of the proposed approach is to convert the ill-posed SR reconstruction problem in the spectral domain to a quadratic optimization problem in the abundance map domain. In order to do so, Markov random field based energy minimization approach is proposed and proved that the solution is quadratic. The proposed approach consists of five main steps. First, the number of endmembers in the scene is determined using virtual dimensionality. Second, the endmembers and their low resolution abundance maps are computed using simplex identification via the splitted augmented Lagrangian and fully constrained least squares algorithms. Third, high resolution (HR) abundance maps are obtained using our proposed maximum a posteriori based energy function. This energy function is minimized subject to smoothness, unity, and boundary constraints. Fourth, the HR abundance maps are further enhanced with texture preserving methods. Finally, HR HSI is reconstructed using the extracted endmembers and the enhanced abundance maps. The proposed method is tested on three real HSI data sets; namely the Cave, Harvard, and Hyperspectral Remote Sensing Scenes and compared with state-of-the-art alternative methods using peak signal to noise ratio, structural similarity, spectral angle mapper, and relative dimensionless global error in synthesis metrics. It is shown that the proposed method outperforms the state of the art methods in terms of quality while preserving the spectral consistency.**

***Index Terms*— Hyperspectral image, super-resolution reconstruction, MAP Framework, quadratic programming.**

I. Introduction

HYPERSPECTRAL sensors acquire images in many narrow spectral bands of the electromagnetic spectrum, which allow us to identify materials from a single pixel. Despite having high spectral resolution, HSIs suffer from low spatial resolution; which degrades the performance in many applications such as target detection and object recognition [1]. Therefore, super-resolution reconstruction (SRR) which converts a low resolution (LR) image into a high resolution (HR) image is an essential research area for hyperspectral imaging.

In recent years, with the advances in hyperspectral imaging systems and the ease of access to the hyperspectral data, great efforts have been made for SRR of HSIs. Commonly, there are two ways of attacking the SRR problem of HSIs. Although, the majority of the works that deal with the SRR problem use auxiliary information such as multiple LR HSIs or a coinciding HR image with low spectral resolution, there are also studies for SRR of HSIs without using any other source of information. In the former case, different auxiliary data are used for SRR. Multiple LR HSIs having sub-pixel shifts with respect to reference LR HSI can be used to find the high frequency details in the HSI [2]–[4]. Moreover, a HR panchromatic, RGB or multispectral image (MSI) can also be used to fuse with a LR HSI to enhance the resolution [5]–[7]. For this fusion problem, although there are approaches that are adapted from existing pan-sharpening methods for MSIs [8], there exist totally new approaches developed for HSIs such as applying hyperspectral unmixing, comprising Bayesian reconstruction or learning a dictionary. In [9], HR image and HR abundances are jointly solved using spectral unmixing and image fusion concepts together. Endmembers of HSI are initialized and a joint projected gradient based minimization is used to alternately unmix the data and update the endmembers and corresponding HR abundance maps. Coupled Nonnegative Matrix Factorization (CNMF) uses unmixing in the fusion process [10]. HSI is unmixed and endmembers are initialized. HSI and MSI are alternately unmixed using the NMF according to the cost functions promoting the data fidelity. HR HSI is reconstructed using spectral signatures and final abundance maps. HySure (hyperspectral super-resolution) combines Bayesian and unmixing approaches together [11]. Different from the previously mentioned fusion methods, HySure imports a vector total variation regularizer to the fusion process. The total variation regularizer is preserving edges while smoothing out noise in homogeneous regions. In [12], a dictionary based SRR is proposed which uses LR HSI to learn a dictionary whose atoms are the endmembers of the scene. A sparse code is approximated by solving a constrained sparse optimization problem. HR HSI is estimated using the originally learned dictionary and the sparse code. Bayesian approaches can also be used in dictionary learning to obtain the endmembers and abundances [13], [14].

Manuscript received November 25, 2017; revised February 19, 2018; accepted February 25, 2018. Date of publication March 9, 2018; date of current version March 26, 2018. The associate editor coordinating the review of this manuscript and approving it for publication was Prof. Jie Liang. *(Corresponding author: Hasan Irmak.)*

H. Irmak is with the Radar and Electronic Warfare Systems Business Sector (REHIS), ASELSAN Inc., 06830 Ankara, Turkey (e-mail: hirmak@aselsan.com.tr).

G. B. Akar is with the Department of Electrical and Electronics Engineering, Middle East Techical University, 06800 Ankara, Turkey (e-mail: bozdagi@metu.edu.tr).

S. E. Yuksel is with the Department of Electrical and Electronics Engineering, Hacettepe University, 06800 Ankara, Turkey (e-mail: eyuksel@ee.hacettepe.edu.tr).

Color versions of one or more of the figures in this paper are available online at http://ieeexplore.ieee.org.

Digital Object Identifier 10.1109/TIP.2018.2814210

Then, Bayesian sparse coding is used to reconstruct the HR HSI.

The main limitation of these approaches is the difficulty in obtaining the additional source of information [15]. The second way is to attack the SRR problem when the observed data is a single frame in which there is only one LR HSI. The SRR problem is more challenging if any other source of information does not exist. In this case, the LR image has fewer measurements than the number of unknown pixels in the HR image making it an ill-posed problem. The single frame methods can be further categorized as learning based and regularization based methods. In learning based methods, high frequency details of HSIs can be learned from the HR training images [16], [17]. In general, the main advantage of learning based methods is that they provide a natural way of obtaining the required image characteristics, yet, training may require long learning times and the performance highly depends on the similarity between the training dataset and the test dataset. There are also studies that use the same LR image for training and do not need any training set or dictionary [18], [19]. On the contrary, regularization based methods for SRR consider the LR image as the prior knowledge of the HR image, and regularize the solution space using prior assumptions. In this approach, the spectral correlation is used between neighboring pixels and it is employed a spatial regularization by this prior knowledge to obtain HR classification maps [20], [21]. The main drawback of this approach is the assignment of every sub-pixel to a single endmember according to zoom factor. However, this assignment causes an information loss in the sub-pixel and the solution ends up having lower performance for SRR. However, recent regularization based studies handle the problem without assigning each sub-pixel to an endmember using different regularizers such as smoothness, low rank, and spectral consistency [22]–[26].

In this study, LR image is also considered as the prior knowledge of the HR image. However, in order to prevent data loss in the SRR, sub-pixels are not assigned to any single endmember while increasing the resolution. Abundance of each endmember is preserved for that sub-pixel in SRR process. In order to find the abundances of endmembers, linear mixture model is used. The SRR problem in the spectral domain is converted into a joint energy minimization problem completely in the abundance domain. By doing so, using quadratic programming techniques, unique solution is found for the HR abundance maps. Using these maps and spectral signatures of the endmembers, HR HSI is reconstructed. Experimental results show that the proposed approach not only performs better than state-of-the art methods, but also keeps the spectral consistency. The rest of the paper is organized as follows: Section 2 describes the methodology of the proposed method, Section 3 gives the quantitative experimental results; and Section 4 presents our conclusions.

II. Proposed Approach

In SRR, a real imaging system relating an HR HSI Z to the LR observation scene Y is defined as the observation model as given in (1). In this observation model, D represents the down sampling operation, B represents the averaging filter for blur operation and n is the additive noise. Here, Z and Y are used in lexicographical representation in which the rows of each spectral image band are concatenated to construct HR HSI (Z) and LR HSI (Y) matrices as given in (2) and (3) for p spectral bands. The relationship between Z and Y can be written as:

$$Y = DBZ + n \tag{1}$$

where

$$Z \triangleq \begin{bmatrix} Z(1) & Z(2) & \cdots & Z(p) \end{bmatrix} \tag{2}$$

$$Y \triangleq \begin{bmatrix} Y(1) & Y(2) & \cdots & Y(p) \end{bmatrix} \tag{3}$$

$Y(p)$ corresponding to the p^{th} band of LR HSI is of length MN and $Z(p)$ corresponding to the p^{th} band of HR HSI is of length $l_1 M l_2 N$ where M and N are the width and height of the single band of the LR HSI, respectively. Also, l_1 and l_2 are the down-sampling factors in vertical and horizontal directions, respectively. D is of size $MN \times l_1 M l_2 N$, B is $l_1 M l_2 N \times l_1 M l_2 N$ and n is of size $MN \times p$.

Using this observation model, the HR HSI estimate can be found by:

$$\widehat{Z}(i) = arg\ min_{Z(i)} ||DBZ(i) - Y(i)||_F^2 \quad i = 1, \ldots, p \tag{4}$$

where F stands for the Frobenius-norm.

SRR of color images, there are widely accepted methods found in the literature [27]–[30]. However, SRR of HSI is a more demanding problem. Because in HSI, the spectral dimensionality of data is huge and developed algorithms should handle these data. Moreover, the difficulty to obtain several LR images enforces to enhance the resolution using single LR HSI. Therefore, adding the prior information is necessary for the single image SRR of HSI.

In hyperspectral imaging, unmixing is an approach to identify pure materials and their fractions in the scene. The spectra of pure materials are called endmembers and their fractions for a given pixel are called the abundance maps of the material. In HSI, abundance of a material in a pixel is closely related to the abundance of neighboring pixels for that material. Therefore, instead of using pixel values, abundances of the endmembers can be used in SRR of HSI. This idea has some main advantages. First, in general, two neighboring pixels have similar fractions for the same endmember [31] which can be used as the smoothness prior to stabilize the ill-posed inverse problem in solution of (4). Moreover, increasing the resolution of abundances can give spectrally more consistent results compared to the pixel based methods. Therefore, instead of solving (4), abundance maps can be used in the SRR process.

Before performing spectral unmixing, a mixing model should be determined. Mixing model describes how the endmembers in a single pixel constitute the pixel spectra. There are two types of mixing models namely linear mixing model (LMM) and non-linear mixing model (NLMM) [32], [33]. In LMM, the main assumption is that proportions of the endmembers in each pixel are well-defined with a single reflection of the illuminating radiation. In other words, spectrum of each pixel in the HSI is a linear combination of

the spectrum of endmembers and can be rewritten using the endmembers and their abundances linearly. On the contrary, the NLMM assumes materials are distributed randomly in the mixed pixel in a homogeneous manner. Multiple reflections exist and linear proportions does not hold for the NLMM model which is more accurate than the LMM model. However, LMM is widely used instead of NLMM because LMM gives an acceptable first order approximation to the observed scene and NLMM is much more difficult and complicated to analyze HSI as compared to LMM [34]. Therefore, in this study, spectral unmixing is applied using the LMM.

Using linear spectral unmixing, the HR image Z (or the LR image Y) can be written as a linear combination of the endmembers based on their abundances. Since both HR and LR HSI capture the same scene, the underlying materials (i.e. endmembers) should be the same [35]. Therefore, the endmember information extracted from one of the images should also be same for the other one. Equations (5) and (6) show the relation between abundances of HR and LR HSIs respectively. Here, P is the endmember matrix, A_z and A_y are the HR and LR abundance map matrices, ε_Z and ε_Y are the residual errors between original image (i.e. Z or Y) and the reconstructed image.

$$Z = A_z P + \varepsilon_Z \tag{5}$$

$$Y = A_y P + \varepsilon_Y \tag{6}$$

$$A_z \triangleq \begin{bmatrix} A_z(1) & A_z(2) & \cdots & A_z(E) \end{bmatrix} \tag{7}$$

$$A_y \triangleq \begin{bmatrix} A_y(1) & A_y(2) & \cdots & A_y(E) \end{bmatrix} \tag{8}$$

where E denotes the number of endmembers in the scene and P is a matrix of size $E \times p$ and each row of P is an endmember. $A_z(e)$ and $A_y(e)$ are the e^{th} column of the matrices A_z and A_y respectively.

Assuming the residual errors ε_Z and ε_Y are very small and plugging (5) and (6) into the minimization problem given in (4), the expression can be written in terms of spectral signatures and abundances of the scene:

$$\widehat{A_z P(i)} = argmin_{A_z P(i)} ||DBA_z P(i) - A_y P(i)||_F^2 \tag{9}$$

where $P(i)$ shows the i^{th} column of the matrix P. In (9), since spectral signature matrix P is constant and if the determinant of P is non-zero then it has no effect on minimization and can be removed. Hence, (9) can be rewritten in a matrix form in (10) or equivalently in a vector form by using summation as given in (11).

$$\widehat{A}_z = argmin_{A_z} ||DBA_z - A_y||_F^2 \tag{10}$$

$$\widehat{A}_z = argmin_{A_z} \sum_{e=1}^{E} ||DBA_z(e) - A_y(e)||_F^2 \tag{11}$$

Thus, in the proposed approach, (11) is minimized. In doing so, the SRR minimization problem could be solved in the abundance map domain, contrary to the spectral domain. However, since the SRR is an ill-posed inverse problem, the data constraint (DC) term in (11) should be regularized with additional constraints. The smoothness constraint (SC) that promotes smooth HR abundances, and the unity constraint (UC) that guarantees the sum of abundances for each pixel in HSI to be equal to one are utilized. Using these constraints with boundaries of the abundances (i.e. boundary constraint (BC)), the total energy function is minimized and solved for the HR abundances of endmembers. In [24]–[26], Irmak *et al.* used the described approach to solve SRR problem for HSIs. In this paper, we use a similar approach to come up with a systematic solution together with additional constraints to increase the performance. The block diagram of whole process is given in Figure 1.

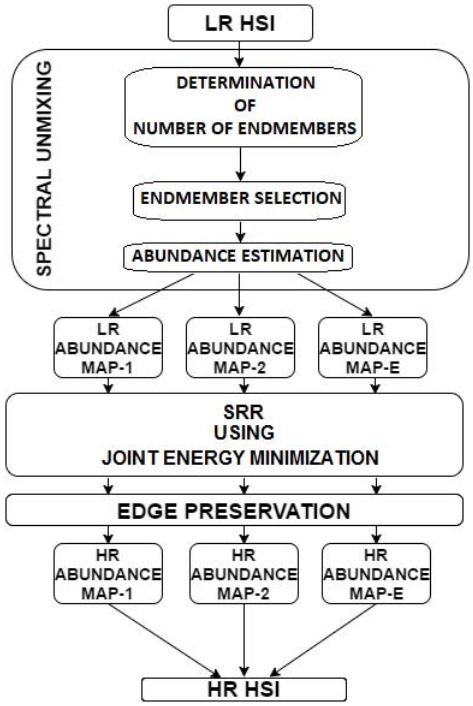

Fig. 1. Block diagram of the proposed method.

Each box in Figure 1 will be explained in detail in the upcoming subsections.

A. Spectral Unmixing

Spectral unmixing is the process of endmember detection and abundance estimation and several unmixing algorithms exist in the literature [32] and [33].. A critical part of unmixing is determining the number of endmembers in the scene. One effective method to accomplish this is through virtual dimensionality (VD), which gives the minimum number of spectrally distinct signal sources that characterize the spectral data [36]–[39]. In this paper, the noise whitened Harsanyi Farrand Chang (NWHFC) method is used to estimate the VD, due to its superior performance in several hyperspectral datasets. The Harsanyi Farrand Chang (HFC) method uses a Neyman-Pearson detection theory based thresholding [40]; and NWHFC is a modified version of HFC with a preprocessing noise whitening step to remove the second order statistical correlation [41].

After the number of endmembers in the scene is determined, the endmembers from hyperspectral data are extracted. Extraction algorithms can be divided into two groups: with or without the assumption that pure pixels are present in the image

for each endmember [42]. Since the pure pixel assumption is a hard constraint for LR images, an endmember detection algorithm without the pure pixel assumption is more suitable for our purposes. Therefore, in this study, a SISAL based algorithm is used for endmember extraction, which was shown to perform better than the competing methods in [43]. In SISAL, unmixing is achieved by finding the minimum volume simplex which contains the hyperspectral data. This optimization problem is solved by a sequence of variable splitting augmented Lagrangian optimizations [44].

Once the endmembers in the scene are extracted, the next step is to estimate the abundances. In the literature, various approaches are proposed [45]. Among these, a FCLS based algorithm has shown the best results to estimate the abundance maps. FCLS is an iterative linear mixture analysis algorithm that finds the abundance maps from the endmember signatures considering the two properties of the abundances. These properties are (i) the sum to one constraint (i.e. sum of abundances for a single pixel is unity), and (ii) the non-negativity constraint (i.e. abundances are non-negative). These abundance maps are called as LR abundance maps throughout the paper; and are used in the SRR process.

B. SRR Using Joint Energy Minimization

Once the LR abundance maps are known, (11) is the basic data cost function for the estimation of the HR abundance maps. However, this is an ill-posed inverse problem which requires a regularization term to find the solution in a stable manner as in (12).

$$C_T = C_D + \lambda C_R \tag{12}$$

Here, C_D is the data cost function, C_R is the regularizer function, C_T is the total cost function and λ adjusts the degree of the regularization.

To simplify the equality, the data cost in (11) can be rewritten as:

$$C_D = z^T D_{DB}^T D_{DB} z - z^T D_{DB}^T y - y^T D_{DB} z + y^T y \tag{13}$$

where

$$z \triangleq \begin{bmatrix} A_z(1) \\ A_z(2) \\ \vdots \\ A_z(E) \end{bmatrix} \tag{14}$$

$$y \triangleq \begin{bmatrix} A_y(1) \\ A_y(2) \\ \vdots \\ A_y(E) \end{bmatrix} \tag{15}$$

$$D_{DB} \triangleq \begin{bmatrix} DB & 0 & \cdots & 0 \\ 0 & DB & \cdots & 0 \\ \vdots & \vdots & \ddots & \vdots \\ 0 & 0 & \cdots & DB \end{bmatrix} \tag{16}$$

In (13), $z^T D_{DB}^T y$ and $y^T D_{DB} z$ are scalar terms and are equal to each other. In addition, $y^T y$ is constant and has no effect on the minimization of the cost function. Therefore, it can be removed; and the final form of C_D is given in (17):

$$C_D = z^T D_{DB}^T D_{DB} z - 2 y^T D_{DB} z \tag{17}$$

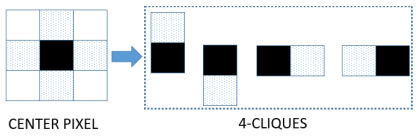

Fig. 2. Cliques for the 4-neighborhood system.

After obtaining the data cost function, the regularization term should be determined. It is known that real world images have slow and sharp changes within the pixel neighborhood. Therefore, the correlation between neighborhood pixels can be used as a prior information in the SRR process. Markov Random Field (MRF) model is a common image prior model which assumes that the physical properties in a neighborhood present a coherency and do not change abruptly [46]. An MRF model constructs the global joint distribution from local neighborhood relations. It is an undirected graph in which the nodes represent the random variables. A node is independent of all other nodes except the neighbor nodes, which are called as cliques. For example, a pixel and its upper neighbor is a clique. Figure 2 shows the 4-neighborhood (up, down, left, right) cliques.

For an HR abundance map $A_z(e)$ of endmember e, the MRF based smoothness regularizer, $C_{R,e}$, states that the abundances in a neighborhood should be close to each other. Therefore, it penalizes the differences within the cliques, and is given in (18):

$$C_{R,e} = \sum_{j=1}^{4} ||A_z(e) - \tilde{A}_{zclique}(e)(j)||_F^2 \tag{18}$$

where $\tilde{A}_{zclique}(e)(j)$ shows the 4-neighborhood pixel vector for endmember e. Expanding the squared expression in (18):

$$\begin{aligned} C_{R,e} = {} & ||A_z(e) - S^u A_z(e)||_F^2 + ||A_z(e) - S^d A_z(e)||_F^2 \\ & + ||A_z(e) - S^l A_z(e)||_F^2 + ||A_z(e) - S^r A_z(e)||_F^2 \end{aligned} \tag{19}$$

In (19), S^u, S^d, S^l, S^r are the shift operations that shift the image one pixel up, down, left and right respectively. Analyzing the first term in (19), it can be rewritten it as:

$$\begin{aligned} ||A_z(e) - S^u A_z(e)||_F^2 &= ||(I - S^u) A_z(e)||_F^2 \\ &= A_z(e)^T (I - S^u)^T (I - S^u) A_z(e) \end{aligned} \tag{20}$$

where I is the identity matrix of size $l_1 M l_2 N \times l_1 M l_2 N$. By using the expansion in (20), (19) can be rewritten as:

$$\begin{aligned} C_{R,e} = {} & A_z(e)^T (I - S^u)^T (I - S^u) A_z(e) \\ & + A_z(e)^T (I - S^d)^T (I - S^d) A_z(e) \\ & + A_z(e)^T (I - S^l)^T (I - S^l) A_z(e) \\ & + A_z(e)^T (I - S^r)^T (I - S^r) A_z(e) \end{aligned} \tag{21}$$

Then, (21) can be extended for all endmembers:

$$C_R = z^T[(I_E - D_S^u)^T(I_E - D_S^u) + (I_E - D_S^d)^T(I_E - D_S^d) + (I_E - D_S^l)^T(I_E - D_S^l) + (I_E - D_S^r)^T(I_E - D_S^r)]z \tag{22}$$

where I_E is the identity matrix of size $El_1Ml_2N \times El_1Ml_2N$ and:

$$D_S^u \triangleq \begin{bmatrix} S^u & 0 & \cdots & 0 \\ 0 & S^u & \cdots & 0 \\ \vdots & \vdots & \ddots & \vdots \\ 0 & 0 & \cdots & S^u \end{bmatrix} \tag{23}$$

$$D_S^d \triangleq \begin{bmatrix} S^d & 0 & \cdots & 0 \\ 0 & S^d & \cdots & 0 \\ \vdots & \vdots & \ddots & \vdots \\ 0 & 0 & \cdots & S^d \end{bmatrix} \tag{24}$$

$$D_S^l \triangleq \begin{bmatrix} S^l & 0 & \cdots & 0 \\ 0 & S^l & \cdots & 0 \\ \vdots & \vdots & \ddots & \vdots \\ 0 & 0 & \cdots & S^l \end{bmatrix} \tag{25}$$

$$D_S^r \triangleq \begin{bmatrix} S^r & 0 & \cdots & 0 \\ 0 & S^r & \cdots & 0 \\ \vdots & \vdots & \ddots & \vdots \\ 0 & 0 & \cdots & S^r \end{bmatrix} \tag{26}$$

Finally, the total cost function C_T in (12) is obtained by combining the cost functions in (17) and (22) with a regularizer coefficient λ. Here, λ adjusts the smoothness degree of the image. Then, C_T is minimized to obtain the HR HSI.

In the minimization procedure, there are two constraints. The first one, the boundary constraint (BC), is that the abundances values, $A_z(e)$, are between zero and one:

$$\underline{0} \leq A_z(e) \leq \underline{1} \;\forall\; e \tag{27}$$

In (27), $\underline{0}$ and $\underline{1}$ are the column vectors of size l_1Ml_2N in which every element is 0 and 1, respectively. The second constraint, the unity constraint (UC), is that the sum of abundances for a single pixel should be unity:

$$UC = \sum_{e=1}^{E} A_z(e) = \underline{1} \tag{28}$$

To convert the problem into a form of quadratic minimization problem, (28) can be written as:

$$A_{eq}z = b_{eq} \tag{29}$$

where

$$A_{eq} \triangleq \begin{bmatrix} I & I & \cdots & I \end{bmatrix} \tag{30}$$

$$b_{eq} \triangleq \underline{1} \tag{31}$$

A_{eq} is of size $l_1Ml_2N \times El_1Ml_2N$ which is constructed by concatenating E number of identity matrices horizontally and b_{eq} is the column vector of size l_1Ml_2N.

With the cost functions, the HR abundance maps are estimated using the C_T in (12) with the BC in (27) and UC in (28). Since UC is a constraint between abundance maps, a joint minimization is required. This minimization problem is quadratic and can be solved using quadratic programming (QP) methods [47]. A general QP problem is in the form:

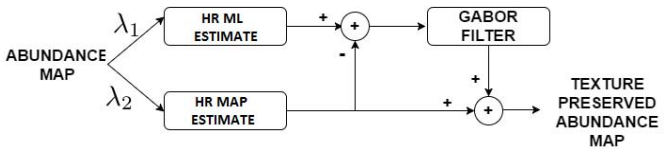

Fig. 3. Block diagram of texture preserving operation.

$$\text{minimize} \quad f(z) = \frac{1}{2}z^T Hz + f^T z \tag{32}$$

$$\text{subject to} \quad A_{eq}z = b_{eq} \tag{33}$$

$$l \leq z \leq h \tag{34}$$

The cost function C_T can be converted to the quadratic form given in (32) with defining H, f, l and h as:

$$H \triangleq 2D_{DB}^T D_{DB} + 2\lambda.[(I_E - D_S^u)^T(I_E - D_S^u) + (I_E - D_S^d)^T(I_E - D_S^d) + (I_E - D_S^r)^T(I_E - D_S^r) + (I_E - D_S^l)^T(I_E - D_S^l)] \tag{35}$$

$$f \triangleq (-2y^T D_{DB})^T \tag{36}$$

$$\underline{0} \leq z \leq \underline{1} \quad (l = \underline{0} \quad and \quad h = \underline{1}) \tag{37}$$

After these rearrangements, the problem can be solved using QP solving techniques such as the interior point method which has been proven to work well in practice [48]. In this study, QP problem is also minimized using the interior point method; and the global minimum point gives the HR abundance maps of the HR HSI.

C. Post Processing to Remove λ Dependency

In the cost function, the value of λ is very critical. Higher λ values oversmooth the image whereas lower λ values preserve the textures but lead energy minimization into an ill-posed inverse problem. Therefore, finding the optimum λ value is a hard problem and instead of using a constant λ, the method suggested by [49] is used to preserve edges and textures. In this method, the SRR problem is solved two times with two different regularization parameters; λ_1 and λ_2 as shown in Figure 3. First, regularization parameter is chosen to be very close to zero (i.e. $\lambda_1 \approx 0$) and it creates a noisy estimate of the image while preserving textures. This solution can be called as the Maximum Likelihood (ML) estimate. On the other hand, the second regularization parameter is chosen to be much greater than the first one ($\lambda_1 \ll \lambda_2$) and creates an over-smoothed SRR estimate. Similarly, it can be called as the MAP estimate. The difference of the first estimate and the second estimate gives the high frequency (HF) image that is composed of edges and textures. Then, Gabor filters in different orientations are applied to this HF image to detect textures. These filters applied to HF image separately and for each filter output, the pixels below a predefined threshold

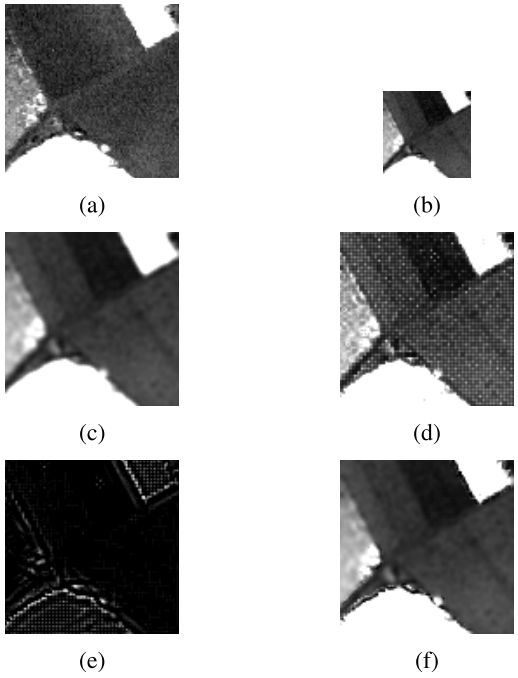

Fig. 4. Texture Preserving example. (a) HR abundance map. (b) LR abundance map. (c) HR map estimate. (d) HR ML estimate. (e) HF abundance map. (f) TP abundance map.

are masked. Then, these masked filter outputs are summed to obtain the restored HF image. Finally, the restored HF image is summed with the MAP estimate to obtain texture preserved (TP) final image. Instead of the image bands, in the proposed method, texture preserving is applied to abundance maps. An example of ML estimate, MAP estimate, HF image and final TP abundance map are given in Figure 4. In this figure, HF image shows the textures in the abundance map and these textures are restored in the final abundance map.

After the smoothness-prior-based energy minimization is performed as discussed in Sec.II-B, this texture preserving operation is applied to restore the details in the image. It is applied to each abundance map; so TP HR abundance maps are obtained for all endmembers. Using these HR abundances and the spectral signature matrix P, final HR HSI is constructed using equation (5).

As a side note, the UC and BC in the energy function are not affected by the texture-preserving operation. Since both the ML and the MAP estimates of the abundances satisfy the UC and BC; summing the unity gain filtered difference of them with MAP estimate also satisfies these constraints. Therefore, TP abundance maps still have the properties of abundance maps of HR HSI.

III. Experimental Results

The proposed method is applied to three different datasets. The first dataset is the Cave dataset which consists of 32 scenes [50]. It is in the 400 nm to 700 nm wavelength range with steps of 10 nm. The second database, called Harvard [51], has 50 indoor and outdoor images recorded under daylight illumination. Images have 31 spectral bands of 10 nm width, ranging from 420 nm to 720 nm. The last dataset is the Hyperspectral Remote Sensing Scenes (HRSS) dataset of urban areas consists of 5 images [52]. The area covered is comprised of images of different sizes, with hundred spectral bands from 380 nm to 2500 nm.

For all the experiments, image patches with size 256x256 are used as the reference image. These HR patches form the ground truth and are used to evaluate the performance of the proposed method. The LR HSI are obtained from these HR images by blurring the HR HSI using a 3x3 averaging filter, down sampling the result by two and adding a 30 dB additive white Gaussian noise signal.

The proposed method is compared with different methods. The first method is the standard bicubic interpolation which is applied to HSI band by band. The second method is called Timofte *et al.*'s [53] method which is a state-of the art single image dictionary based SRR method. For the training samples, ten percent of the HSIs are used for each dataset with patch size of 256x256, dictionary size of 1024, and a neighborhood size of 2048. The last two methods are the two recent single image SRR methods for HSIs; which will be referred to as the Xu *et al.* [22] and the Li *et al.* [19] from now on. Xu *et al.*'s method is a very recent regularization based single image SRR method for HSIs. Li *et al.*'s method is a dictionary based hyperspectral SRR method; which was shown to have a better performance than several other hyperspectral SRR methods [19]. In the experimental results, the proposed approach is compared to both of these studies with or without the post-processing stage described in Sec.II-C. In the rest of the paper, our results without the post-processing stage will be referred to as the "MAP w/o post-processing" and the results after the post-processing stage will be referred to as the "MAP w post-processing". In both methods, the same regularization parameter (i.e. λ) value is used to find the MAP estimate. The value is determined heuristically using the datasets.

The algorithms are compared quantitatively using four measures: (i) peak signal-to-noise ratio (PSNR), (ii) structural similarity index measure (SSIM), (iii) spectral angle mapper (SAM) and (iv) relative dimensionless global error in synthesis (ERGAS). The first measure, PSNR, is the ratio between the maximum possible power of a signal and the power of the distorting noise [54]. Given an estimated image y and a reference image x, PSNR is computed as:

$$PSNR(x, y) = 10\log_{10}\left(\frac{(MAX_I)^2}{\frac{1}{mn}\sum_{i=0}^{m-1}\sum_{j=0}^{n-1}[x(i,j)-y(i,j)]^2}\right) \tag{38}$$

where MAX_I is the maximum intensity in the reference image.

The second measure, SSIM, is based on the human visual perception which is more sensitive to structural information [55]. The SSIM is defined as:

$$SSIM(x, y) = \frac{(2\mu_x\mu_y + C_1)(2\sigma_{xy} + C_2)}{(\mu_x{}^2\mu_y{}^2 + C_1)(\sigma_x{}^2 + \sigma_y{}^2 + C_2)} \tag{39}$$

TABLE I
EXPERIMENTAL RESULTS FOR THE CAVE DATASET

	PSNR	SSIM	SAM	ERGAS
Bicubic Interpolation	30.866	0.900	6.881	38.907
Timofte *et al.* [53]	34.522	0.921	4.900	28.210
Xiong *et al.* [22]	32.063	0.916	6.306	36.285
Jie *et al.* [19]	34.244	0.891	5.367	30.917
MAP w/o post-processing	34.459	0.931	4.757	27.202
MAP w. post-processing	**34.913**	**0.932**	**4.643**	**26.491**

TABLE II
EXPERIMENTAL RESULTS FOR THE HARVARD DATASET

	PSNR	SSIM	SAM	ERGAS
Bicubic Interpolation	28.734	0.811	6.447	28.988
Timofte *et al.* [53]	32.713	0.840	4.400	19.556
Xiong *et al.* [22]	30.452	0.830	5.561	25.028
Jie *et al.* [19]	31.647	0.817	5.314	24.712
MAP w/o post-processing	32.711	**0.858**	4.357	19.886
MAP w. post-processing	**32.898**	0.855	**4.299**	**19.494**

where μ_x and μ_y are the mean values of the pixels in a window for images x and y. σ_x^2, σ_y^2 and σ_{xy} are the variances of x, y and the covariance of x and y respectively. C_1 and C_2 are two constants used to avoid instability, and are set to 0.01 and 0.03 respectively as in [55].

The third measure, SAM, is the angle between the estimated i^{th} pixel $x(i)$ and the ground truth i^{th} pixel $y(i)$, averaged over the whole image [56]. The SAM is given in (40) where N is the number of pixels in the image. It measures the average spectral distortion in radians between two images.

$$SAM(x, y) = \frac{1}{N} \sum \arccos \frac{x(i)^T y(i)}{||x(i)||_2 ||y(i)||_2} \tag{40}$$

Last measure is ERGAS which is used to measure the radiometric distortion in the images [57]. The main difference between SAM and ERGAS is that the former is used to measure spectral distortion whereas the latter is concerned with the radiometric distortion. Therefore, both metrics are the most common metrics for quantitative comparisons in HSI applications.

$$ERGAS(x, y) = \frac{100}{SR} \sqrt{\frac{1}{p} \sum_{i=1}^{p} \left(\frac{RMSE(x_i, y_i)}{\mu_i} \right)^2} \tag{41}$$

where p is the total number of bands, SR is the scale ratio between LR and HR images, $RMSE$ is the root mean square error function and μ_i is the average of the i^{th} band. A zero ERGAS value denotes the absence of radiometric distortion, but possible spectral distortion.

In these metrics, while higher PSNR and SSIM measures indicate a better match between the estimation and the ground truth; lower SAM and ERGAS values are desired for smaller distortions.

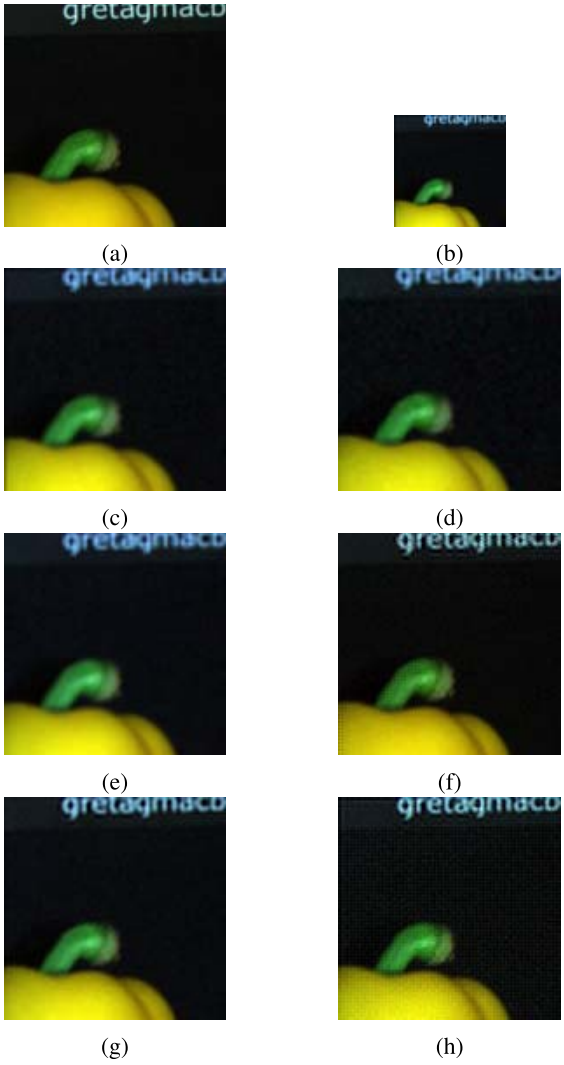

Fig. 5. Experimental results on the cave dataset. (a) HR original image. (b) LR image. (c) Bicubic interpolation. (d) Timofte *et al.* (e) Xiong *et al.* (f) Jie *et al.* (g) MAP w/o post-processing. (h) MAP w. post-processing.

All three datasets are tested with these performance metrics. The mean of the results of all images for each dataset are given in Tables I–III. Upon observing the results, in all datasets, both MAP without post-processing and MAP with post-processing approach outperform the other methods nearly in all metrics. MAP with post-processing approach has slightly better performance in all metrics and datasets as compared to MAP without post-processing. The proposed approaches have superior performance in HRSS dataset in which HSIs have more than hundreds of bands. This is particularly critical in remote sensing applications where HSI consists of hundreds of bands.

For visual comparison, in Figures 5–7 RGB images are given using red, green and blue bands of HSI. Visual results show that our proposed approaches are better than the both methods. The effect of edge preservation can be seen in these figures. MAP with the post-processing preserves the edges and textures as compared to the MAP without the post-processing.

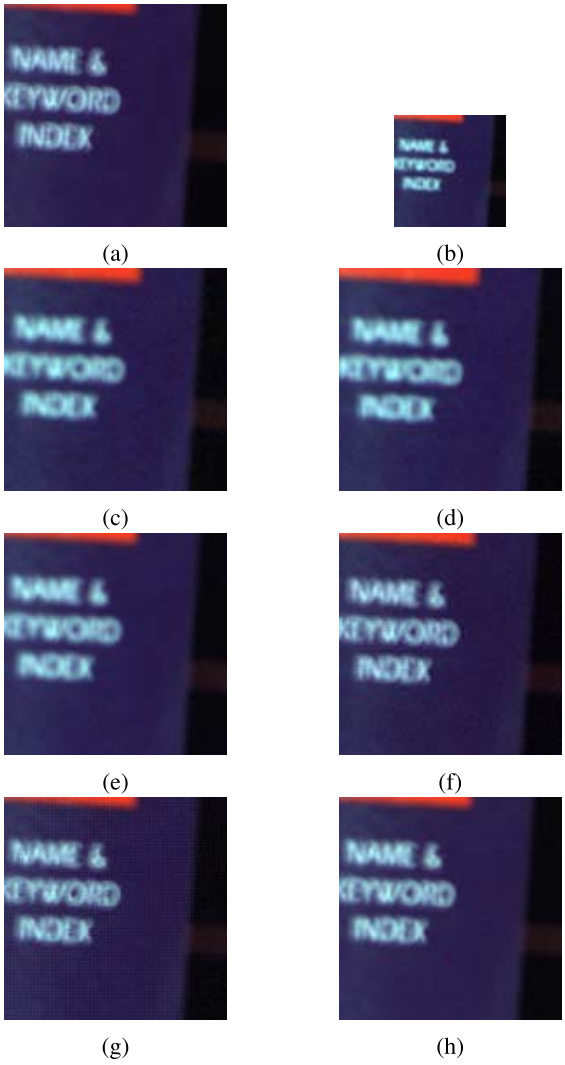

Fig. 6. Experimental results on the Harvard dataset. (a) HR original image. (b) LR image. (c) Bicubic interpolation. (d) Timofte *et al.* (e) Xiong *et al.* (f) Jie *et al.* (g) MAP w/o post-processing. (h) MAP w. post-processing.

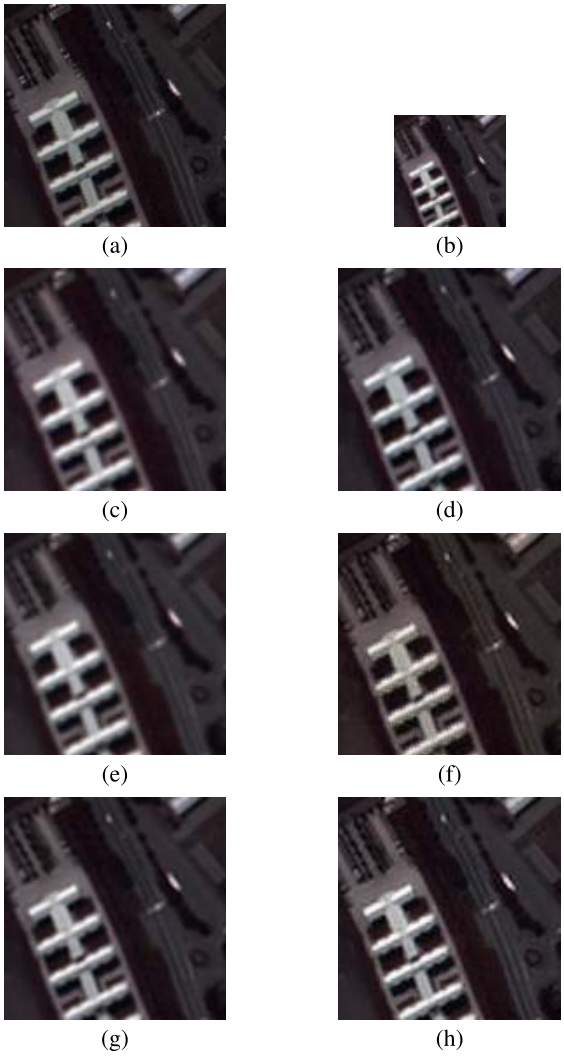

Fig. 7. Experimental results on the HRSS dataset. (a) HR original image. (b) LR image. (c) Bicubic interpolation. (d) Timofte *et al.* (e) Xiong *et al.* (f) Jie *et al.* (g) MAP w/o post-processing. (h) MAP w. post-processing.

TABLE III
EXPERIMENTAL RESULTS FOR THE HRSS DATASET

	PSNR	SSIM	SAM	ERGAS
Bicubic Interpolation	26.413	0.791	7.111	29.324
Timofte *et al.* [53]	29.665	0.852	5.957	24.941
Xiong *et al.* [22]	27.951	0.820	6.306	27.046
Jie *et al.* [19]	30.230	0.817	5.139	22.198
MAP w/o post-processing	30.375	**0.876**	4.873	**21.243**
MAP w. post-processing	**30.443**	0.874	**4.851**	21.248

Spectral consistency is another important issue in SRR of HSI. The spectral characteristics of an average of 8-neighborhood pixels of the center pixel of the one of the HRSS image (i.e. region shown with the white box in Figure 8) are calculated from the results of the four compared algorithms. The results are given in Figure 9 between

Fig. 8. Spectral consistency calculation region.

the bands from 1 to 50 for better visuality. As seen from Figure 9, the ground truth and our proposed methods are nearly overlapped. However, bicubic interpolation and Xiong *et al.* methods highly degrade the spectrum consistency. Moreover, Timofte *et al.* and Jie *et al.* have better performance than bicubic interpolation and Xiong *et al.* but corrupt the bands from 45 to 50. RMSE between the ground truth and SRR methods are also calculated using average of 8-neighborhood pixels of the center pixel of the image and given in Table IV. One can see that the proposed methods have better spectral consistency as compared with the other SRR methods.

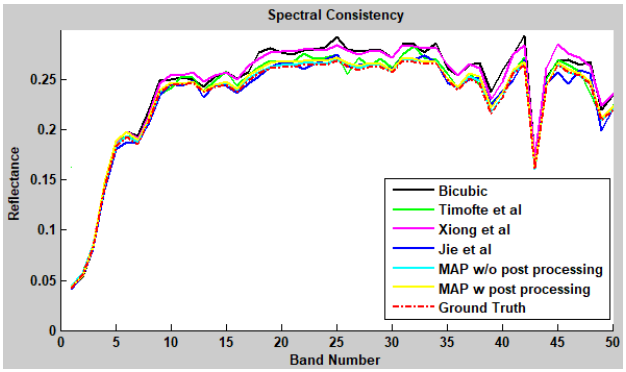

Fig. 9. Spectral reflectance characteristics of HRSS dataset for different SRR methods.

TABLE IV
RMSE IN SPECTRAL REFLECTANCE BETWEEN GROUND TRUTH AND SRR METHODS

	Bicubic Interpolation	Timofte *et al.* [53]	Xiong *et al.* [22]	Jie *et al.* [19]	MAP w/o post-processing	MAP w. post-processing
RMSE	4.6548	2.3971	4.3663	1.6325	**0.7308**	1.2102

Lastly, MATLAB is used in the implementation of the algorithm. The implementation is not optimized for speed and computation time depends on the number of endmembers. In the experiments, the estimated number of endmembers are typically between 3 and 10 and the average computation time is around 6 minutes for MAP without post-processing and 12 minutes for MAP with post-processing on a single i7 quad core 2.2 GHz CPU for a single HSI SRR. Moreover, memory requirement is optimized using sparse matrices in the implementation. For example, H matrix, which has the highest memory requirement in the implementation, requires 171 MB memory for 10 endmembers, 256x256 image and 3x3 averaging blur and total memory requirements is below 2 GB for the implementation.

IV. CONCLUSION

In this work, a novel MAP based SRR method for HSIs is presented. The idea of the proposed approach is that instead of using the spectral images, the correlation of neighboring pixels in terms of abundances of the endmembers and their properties in the scene are used in the SRR process to form a quadratic optimization problem in the abundance map domain. Moreover, QP problem is solved jointly with constraints specific to abundance maps results in more stable solutions. Another advantage of using the abundances in SRR process is obtaining spectrally more consistent results in HR HSI. In the proposed approach, first, hyperspectral data is unmixed and abundances of the endmembers are found. Then, using the LR abundance maps as the basic DC, an energy function is defined using an SC from a priori information with a UC and a BC for the abundance maps. This energy function is jointly minimized using QP. Moreover, in order to preserve textures, a post processing is applied to the HR abundance maps. Proposed approach is tested on three real hyperspectral datasets and compared to other state-of-the-art SRR methods. The results show that the proposed algorithm produces better results in all PSNR, SSIM, SAM and ERGAS metrics compared to other techniques. In addition, upon observing the individual pixels for spectral consistency, the proposed method is closest to the ground truth in the experiments.

ACKNOWLEDGEMENT

The authors would like to thank Jie Li for providing the source code for [19].

REFERENCES

[1] Y. Gu, Y. Zhang, and J. Zhang, "Integration of spatial–spectral information for resolution enhancement in hyperspectral images," *IEEE Trans. Geosci. Remote Sens.*, vol. 46, no. 5, pp. 1347–1358, May 2008.
[2] Q. Wang and W. Shi, "Utilizing multiple subpixel shifted images in subpixel mapping with image interpolation," *IEEE Geosci. Remote Sens. Lett.*, vol. 11, no. 4, pp. 798–802, Apr. 2014.
[3] L. Su, S. Zhou, and Y. Yuan, "High spatial resolution image restoration from subpixel-shifted hyperspectral images," *J. Appl. Remote Sens.*, vol. 9, no. 1, p. 095093, 2015.
[4] J. C.-W. Chan, J. Ma, and F. Canters, "A comparison of superresolution reconstruction methods for multi-angle chris/proba images," *Proc. SPIE*, vol. 7109, p. 710904, Oct. 2008.
[5] Y. Zhao, Y. Yang, Q. Zhang, J. Yang, and J. Li, "Hyperspectral imagery super-resolution by image fusion and compressed sensing," in *Proc. IEEE Int. Geosci. Remote Sens. Symp. (IGARSS)*, Jul. 2012, pp. 7260–7262.
[6] H. Kwon and Y.-W. Tai, "RGB-guided hyperspectral image upsampling," in *Proc. IEEE Int. Conf. Comput. Vis.*, Dec. 2015, pp. 307–315.
[7] C. Kwan, J. H. Choi, S. Chan, J. Zhou, and B. Budavari, "Resolution enhancement for hyperspectral images: A super-resolution and fusion approach," in *Proc. IEEE Int. Conf. Acoust., Speech Signal Process. (ICASSP)*, Mar. 2017, pp. 6180–6184.
[8] L. Loncan *et al.*, "Hyperspectral pansharpening: A review," *IEEE Trans. Geosci. Remote Sens.*, vol. 3, no. 3, pp. 27–46, Sep. 2015.
[9] C. Lanaras, E. Baltsavias, and K. Schindler, "Hyperspectral super-resolution by coupled spectral unmixing," in *Proc. IEEE Int. Conf. Comput. Vis.*, Dec. 2015, pp. 3586–3594.
[10] N. Yokoya, T. Yairi, and A. Iwasaki, "Coupled nonnegative matrix factorization unmixing for hyperspectral and multispectral data fusion," *IEEE Trans. Geosci. Remote Sens.*, vol. 50, no. 2, pp. 528–537, Feb. 2012.
[11] M. Simoes, J. Bioucas-Dias, L. B. Almeida, and J. Chanussot, "A convex formulation for hyperspectral image superresolution via subspace-based regularization," *IEEE Trans. Geosci. Remote Sens.*, vol. 53, no. 6, pp. 3373–3388, Jun. 2015.
[12] N. Akhtar, F. Shafait, and A. Mian, "Sparse spatio-spectral representation for hyperspectral image super-resolution," in *Proc. Eur. Conf. Comput. Vis.*, 2014, pp. 63–78.
[13] N. Akhtar, F. Shafait, and A. Mian, "Bayesian sparse representation for hyperspectral image super resolution," in *Proc. IEEE Conf. Comput. Vis. Pattern Recognit.*, Jun. 2015, pp. 3631–3640.
[14] N. Akhtar, F. Shafait, and A. Mian, "Hierarchical beta process with Gaussian process prior for hyperspectral image super resolution," in *Proc. Eur. Conf. Comput. Vis.*, 2016, pp. 103–120.
[15] Y. Yuan, X. Zheng, and X. Lu, "Hyperspectral image superresolution by transfer learning," *IEEE J. Sel. Topics Appl. Earth Observ. Remote Sens.*, vol. 10, no. 5, pp. 1963–1974, May 2017.
[16] H. Huang, J. Yu, and W. Sun, "Super-resolution mapping via multi-dictionary based sparse representation," in *Proc. IEEE Int. Conf. Acoust., Speech Signal Process. (ICASSP)*, May 2014, pp. 3523–3527.
[17] J. Hu, Y. Li, and W. Xie, "Hyperspectral image super-resolution by spectral difference learning and spatial error correction," *IEEE Geosci. Remote Sens. Lett.*, vol. 14, no. 10, pp. 1825–1829, Oct. 2017.
[18] F. A. Mianji, Y. Gu, Y. Zhang, and J. Zhang, "Enhanced self-training superresolution mapping technique for hyperspectral imagery," *IEEE Geosci. Remote Sens. Lett.*, vol. 8, no. 4, pp. 671–675, Jul. 2011.
[19] J. Li, Q. Yuan, and H. Shen, "Hyperspectral image super-resolution by spectral mixture analysis and spatial–spectral group sparsity," *IEEE Geosci. Remote Sens. Lett.*, vol. 13, no. 9, pp. 1250–1254, Sep. 2016.

[20] A. Villa, J. Chanussot, J. A. Benediktsson, M. Ulfarsson, and C. Jutten, "Super-resolution: An efficient method to improve spatial resolution of hyperspectral images," in *Proc. IEEE Int. Geosci. Remote Sens. Symp. (IGARSS)*, Jul. 2010, pp. 2003–2006.
[21] Z. Guo, T. Wittman, and S. Osher, "L1 unmixing and its application to hyperspectral image enhancement," *Proc. SPIE*, vol. 7334, p. 73341M, Apr. 2009.
[22] X. Xu *et al.*, "Hyperspectral image super resolution reconstruction with a joint spectral-spatial sub-pixel mapping model," in *Proc. IEEE Int. Geosci. Remote Sens. Symp. (IGARSS)*, Jul. 2016, pp. 6129–6132.
[23] S. He, H. Zhou, Y. Wang, W. Cao, and Z. Han, "Super-resolution reconstruction of hyperspectral images via low rank tensor modeling and total variation regularization," in *Proc. IEEE Int. Geosci. Remote Sens. Symp. (IGARSS)*, Jul. 2016, pp. 6962–6965.
[24] H. Irmak, G. B. Akar, and S. E. Yüksel, "A map-based approach to resolution enhancement of hyperspectral images," in *Proc. 7th IEEE Workshop Hyperspectral Image Signal Process. Evol. Remote Sens. (WHISPERS)*, Jun. 2015, pp. 1–4.
[25] H. Irmak, G. B. Akar, S. E. Yuksel, and H. Aytaylan, "Super-resolution reconstruction of hyperspectral images via an improved MAP-based approach," in *Proc. IEEE Int. Geosci. Remote Sens. Symp. (IGARSS)*, Jul. 2016, pp. 7244–7247.
[26] H. Irmak, G. B. Akar, and S. E. Yüksel, "Hyperspectral imagery super-resolution," in *Proc. 24th Signal Process. Commun. Appl. Conf. (SIU)*, May 2016, pp. 1057–1060.
[27] J. Yang, J. Wright, T. S. Huang, and Y. Ma, "Image super-resolution via sparse representation," *IEEE Trans. Image Process.*, vol. 19, no. 11, pp. 2861–2873, Nov. 2010.
[28] L. Ziwei, W. Chengdong, C. Dongyue, Q. Yuanchen, and W. Chunping, "Overview on image super resolution reconstruction," in *Proc. IEEE 26th Chin. Control Decision Conf. (CCDC)*, May/Jun. 2014, pp. 2009–2014.
[29] R. Timofte, R. Rothe, and L. Van Gool, "Seven ways to improve example-based single image super resolution," in *Proc. IEEE Conf. Comput. Vis. Pattern Recognit.*, Jun. 2016, pp. 1865–1873.
[30] C. Dong, C. C. Loy, K. He, and X. Tang, "Image super-resolution using deep convolutional networks," *IEEE Trans. Pattern Anal. Mach. Intell.*, vol. 38, no. 2, pp. 295–307, Feb. 2015.
[31] M.-D. Iordache, J. Bioucas-Dias, and A. Plaza, "Total variation spatial regularization for sparse hyperspectral unmixing," *IEEE Trans. Geosci. Remote Sens.*, vol. 50, no. 11, pp. 4484–4502, Nov. 2012.
[32] N. Keshava, "A survey of spectral unmixing algorithms," *Lincoln Lab. J.*, vol. 14, no. 1, pp. 55–78, 2003.
[33] J. M. Bioucas-Dias *et al.*, "Hyperspectral unmixing overview: Geometrical, statistical, and sparse regression-based approaches," *IEEE J. Sel. Topics Appl. Earth Observ. Remote Sens.*, vol. 5, no. 2, pp. 354–379, Apr. 2012.
[34] N. Dobigeon, Y. Altmann, N. Brun, and S. Moussaoui, "Linear and nonlinear unmixing in hyperspectral imaging," in *Data Handling in Science and Technology*, vol. 30. Amsterdam, The Netherlands: Elsevier, 2016, ch. 6, pp. 185–224.
[35] M. A. Veganzones, M. Simões, G. Licciardi, N. Yokoya, J. M. Bioucas-Dias, and J. Chanussot, "Hyperspectral super-resolution of locally low rank images from complementary multisource data," *IEEE Trans. Image Process.*, vol. 25, no. 1, pp. 274–288, Jan. 2016.
[36] C.-I. Chang, "Virtual dimensionality for hyperspectral imagery," *Proc. SPIE*, vol. 10, no. 2, p. 1749, 2009.
[37] W. Xiong, C.-I. Chang, and C.-T. Tsai, "Estimation of virtual dimensionality in hyperspectral imagery by linear spectral mixture analysis," in *Proc. Int. Geosci. Remote Sens. Symp. (IGARSS)*, Jul. 2010, pp. 979–982.
[38] J. Bioucas-Dias and J. Nascimento, "Hyperspectral subspace identification," *IEEE Trans. Geosci. Remote Sens.*, vol. 46, no. 8, pp. 2435–2445, Aug. 2008.
[39] M. G. Asl and B. Mojaradi, "Virtual dimensionality estimation in hyperspectral imagery based on unsupervised feature selection," *ISPRS, Ann. Photogram., Remote Sens. Spatial Inf. Sci.*, vol. 3, no. 17, pp. 17–23, 2016.
[40] J. Harsanyi, W. Farrand, and C.-I. Chang, "Determining the number and identity of spectral endmembers: An integrated approach using Neyman-Pearson eigen-thresholding and iterative constrained RMS error minimization," in *Proc. Thematic Conf. Geologic Remote Sens.*, vol. 1. 1993, p. 395.
[41] C.-I. Chang and Q. Du, "Estimation of number of spectrally distinct signal sources in hyperspectral imagery," *IEEE Trans. Geosci. Remote Sens.*, vol. 42, no. 3, pp. 608–619, Mar. 2004.
[42] P. J. Martínez, R. M. Pérez, A. Plaza, P. L. Aguilar, M. C. Cantero, and J. Plaza, "Endmember extraction algorithms from hyperspectral images," *Ann. Geophysics*, vol. 49, no. 1, pp. 93–101, 2006.
[43] J. Plaza, E. M. T. Hendrix, I. García, G. Martín, and A. Plaza, "On endmember identification in hyperspectral images without pure pixels: A comparison of algorithms," *J. Math. Imag. Vis.*, vol. 42, nos. 2–3, pp. 163–175, 2012.
[44] J. M. Bioucas-Dias, "A variable splitting augmented Lagrangian approach to linear spectral unmixing," in *Proc. 1st Workshop Hyperspectral Image Signal Process., Evol. Remote Sens.*, Aug. 2009, pp. 1–4.
[45] D. C. Heinz and C.-I. Chang, "Fully constrained least squares linear spectral mixture analysis method for material quantification in hyperspectral imagery," *IEEE Trans. Geosci. Remote Sens.*, vol. 39, no. 3, pp. 529–545, Mar. 2001.
[46] S. Z. Li, "Markov random field models in computer vision," in *Proc. Eur. Conf. Comput. Vis.*, 1994, pp. 361–370.
[47] P. A. Jensen and J. F. Bard, "Nonlinear programming methods. S2 quadratic programming," in *Operations Research Models and Methods*, vol. 1. Hoboken, NJ, USA: Wiley, 2003, ch. 10.
[48] T. R. Krüth, "Interior-point algorithms for quadratic programming," M.S. thesis, Dept. Inform. Math. Model., Tech. Univ. Denmark, Lyngby, Denmark, 2008.
[49] E. Turgay and G. B. Akar, "Texture and edge preserving multiframe super-resolution," *IET Image Process.*, vol. 8, no. 9, pp. 499–508, Sep. 2014.
[50] F. Yasuma, T. Mitsunaga, D. Iso, and S. K. Nayar, "Generalized assorted pixel camera: Postcapture control of resolution, dynamic range, and spectrum," *IEEE Trans. Image Process.*, vol. 19, no. 9, pp. 2241–2253, Sep. 2010.
[51] A. Chakrabarti and T. Zickler, "Statistics of real-world hyperspectral images," in *Proc. IEEE Conf. Comput. Vis. Pattern Recognit.*, Jun. 2011, pp. 193–200.
[52] *Hyperspectral Remote Sensing Scenes*. Accessed: Sep. 5, 2016. [Online]. Available: http://www.ehu.eus/ccwintco/index.php?title=Hyperspectral_Remote_Sensing_Scenes
[53] R. Timofte, V. De Smet, and L. Van Gool, "A+: Adjusted anchored neighborhood regression for fast super-resolution," in *Proc. Asian Conf. Comput. Vis.*, 2014, pp. 111–126.
[54] J. Moreno, B. Jaime, and S. Saucedo, "Towards no-reference of peak signal to noise ratio," *Int. J. Adv. Comput. Sci. Appl.*, vol. 4, no. 1, pp. 123–130, Jan. 2013.
[55] Z. Wang, A. C. Bovik, H. R. Sheikh, and E. P. Simoncelli, "Image quality assessment: From error visibility to structural similarity," *IEEE Trans. Image Process.*, vol. 13, no. 4, pp. 600–612, Apr. 2004.
[56] S. Rashmi, S. Addamani, and S. Ravikiran, "Spectral angle mapper algorithm for remote sensing image classification," *Int. J. Innov. Sci., Eng. Technol.*, vol. 50, no. 4, pp. 201–205, 2014.
[57] T. Stathaki, *Image Fusion: Algorithms and Applications*. Cambridge, MA, USA: Academic, 2011.

Hasan Irmak, photograph and biography not available at the time of publication.

Gozde Bozdagi Akar, photograph and biography not available at the time of publication.

Seniha Esen Yuksel, photograph and biography not available at the time of publication.